

Synthesis of Fibrous Phosphorus Micropillar Arrays with Pyro-Phototronic Effects

Shuai Zhang,^[a,b] Shufang Ma,^{*[a]} Ben Cao,^[d] Qiandong Zhuang,^[e] Yang Xu,^[c] Jiahui Wang,^[a,b] Xishuo Zhang,^[a,b] Xiaoye Nan,^[b] Xiaodong Hao,^[a] and Bingshe Xu^{*[a,c]}

Dedication ((optional))

-
- [a] Dr. S. Zhang, Prof. Dr. S. F. Ma, J. H. Wang, X. S. Zhang, Prof. X. D. Hao, Prof. Dr. B. S. Xu
Materials Institute of Atomic and Molecular Science
Shaanxi University of Science and Technology
Xi'an, Shaanxi, China, 710021
E-mail: xubingshe@sust.edu.cn, and mashufang@sust.edu.cn.
- [b] Dr. S. Zhang, Dr. J. H. Wang, X. S. Zhang, X. Y. Nan
School of Materials Science and Engineering
Shaanxi University of Science and Technology
Xi'an, Shaanxi, China, 710021
- [c] Dr. Y. Xu, Prof. Dr. B. S. Xu
Key Laboratory of Interface Science and Engineering in Advanced Materials of Ministry of Education
Taiyuan University of Technology
Taiyuan, Shanxi, China, 030024
- [d] Dr. B. Cao
State Key Laboratory of Luminescent Materials and Devices
School of Materials Science and Engineering
South China University of Technology
Guangzhou, 510640, China.
- [e] Prof. Dr. Q. D. Zhuang
Semiconductor Physics & Nanostructures Physics Department
Lancaster University
Lancaster LA1 4YB, UK.

Supporting information for this article is given via a link at the end of the document.

Abstract: The bottom-up preparation of two-dimensional material micro-nano structures at scale facilitates the realisation of integrated applications in optoelectronic devices. Fibrous Phosphorus (FP), an allotrope of black phosphorus (BP), as a two-dimensional layered semiconductor with high anisotropy and catalytic activity, is one of the most promising candidate materials in the field of optoelectronics.^[1] However, to date, there are no bottom-up micro-nano structure preparation methods for crystalline phosphorus allotropes.^[1c, 2] Herein, we present the bottom-up preparation of FP micropillar arrays via a low-pressure gas-phase transport (LP-CVT) method that controls the directional phase transition from amorphous red phosphorus (ARP) to FP. In addition, self-powered photodetectors (PD) of FP-MP arrays with pyro-phototronic effects achieved detection beyond the bandgap limit. Our results provide a new approach for the bottom-up preparation of other phosphorus crystal allotropes.

Fibrous phosphorus (FP), also known as red phosphorus type IV, is an allotrope of elemental phosphorus with good linear/nonlinear optical anisotropy and a high emission yield, properties that stem from its crystal structure in which two coupled parallel tubular chains are bound to each other in the a and c crystallographic directions by covalent interactions and van der Waals (vdW) forces, respectively.^[1b, 1c, 3] Furthermore, experimental studies and calculations both predict that FP possesses catalytic activity and carrier mobility properties comparable to those of black phosphorus (BP), making it an ideal candidate for two-dimensional photo(electro)catalytic, photoelectric applications.^[1d-f, 3c, 4] However, the lack of effective

solutions for the controlled large-scale growth of micro-nano structures of other crystalline phosphorus allotropes including type-II, FP, Hittorf's phosphorus, [P12(4)]P2, and BP has greatly hindered further research and their practical application.^[1a, 1c, 3c, 5] To date, the preparation of FP microstructures has been limited to top-down shedding of bulk parent structures.^[1f, 2e, 4a, 4b] Such methods are not only limited by scale but also by the inevitable surface and crystal structure damage caused by solution residues during liquid stripping.

The bottom-up preparation of micro-nano structures has always been a major challenge.^[6] Recently, studies on the large-scale preparation of BP films by allotropic transformation of red phosphorus, epitaxial nucleation design and pulsed laser deposition (PLD) have laid a solid foundation for the production of BP micro-nano structures,^[2a-c] which however cannot be directly transferred to FP. For example, the uniqueness of the high-temperature and high-pressure devices used in the allotropic transformation method of red phosphorus was not universal; Secondly, the open nature of the FP nucleation mechanism made it not yet applicable to epitaxial nucleation-based synthesis; Furthermore, the PLD strategy was based on a top-down approach, and although its proposal could make the preparation of FP thin films a possibility after fine device tuning, it would obviously make the material the preparation of the material to become convoluted. Herein, we report a self-assembly strategy using amorphous red phosphorus (ARP) as the starting material for the synthesis of high-quality large-scale fibrous phosphorus micropillar (FP-MP) arrays. In contrast to conventional mineraliser-assisted preparation of crystalline

phosphorus,^[2c-e, 7] the directional transformation of ARP facilitates large-scale deposition via **low pressure chemical vapour-phase transport (LP-CVT)** (Figure 1a). In addition to illustrating that the directional transformation of ARP can lead to the formation of large-area homogeneous FP-MP arrays, we also prepared FP-MP array photodetectors (PD) with attractive pyro-phototronic properties as self-powered optoelectronic devices. These results lay the foundation for the application of FP semiconductor integrated circuits in the information industry.

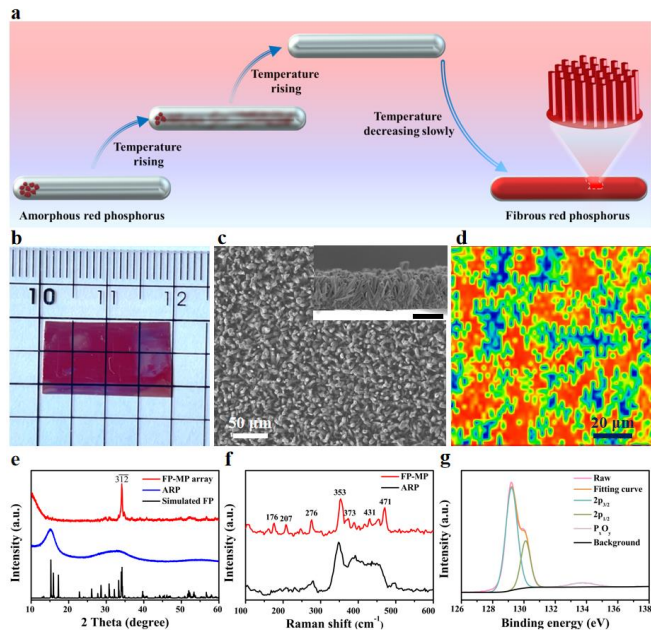


Figure 1. Preparation and characterisation of FP-MP array. (a) Schematic diagram of the synthesis process of the FP-MP array. (b) Photograph of centimetre-scale FP-MP array. (c) SEM image of the FP-MP array. The inset is the SEM image of the FP-MP array cross section. Scale bar, 50 μm . (d) Raman mapping of FP-MP array. (e) XRD patterns of ARP and FP-MPs. (f) Raman spectra of ARP and FP-MP. (g) FP-MP array P 2p XPS results.

We were able to grow centimetre-scale FP-MP arrays in vacuum-sealed ampoules using bulk ARP as precursor (Figure 1b; Supporting Information). The success of a large number of replicate and scale-up experiments suggests that this method has excellent potential for the future fabrication of large-scale device arrays (Figure S2). The use of a directional phase transition from the ARP structure to obtain FP-MPs avoids mineraliser-induced nucleation aggregation and provides a break-through for the bottom-up self-assembled synthesis of micro-nano structures. Combined **scanning electron microscope (SEM)** images and cross section reveal the average FP-MP diameter of 4.06 μm and height of approximately 60 μm (Figure S3 and Figure 1c), with a large aspect ratio. In order to verify that the prepared FP-MPs consist of a single FP phase, **X-ray diffraction (XRD)** and Raman spectroscopy measurements were carried out. The XRD pattern of ARP (Figure 1e) shows three broad peaks at approximately 15°, 32°, and 55°, which are typical of ARP.^[1b, 6b] The XRD pattern of the FP-MP array exhibits a sharp single peak at 34.13°, which coincides with the (3 $\bar{1}\bar{2}$) plane of the ICSD 391323 phase.^[3a, 3b] In addition, the powder XRD pattern (Figure S4) is consistent with the sample consisting of the triclinic FP phase,^[1c, 2e] with no other impurity

peaks, indicating that the transition from ARP to single-phase FP occurred. Furthermore, the Raman spectra of the FP-MPs included complex vibrational features, which may arise from the low symmetry of the triclinic crystal system and coordination between different atoms within the cell.^[1c, 3a, 8] Due to the bending and stretching vibrations of the phosphorus bonds in the tubular structure, distinct peaks appear at 353 cm^{-1} , 373 cm^{-1} , and 470 cm^{-1} . Further, Raman mapping (Figure 1d) and photoluminescence mapping spectrograms revealed that the FP-MP array has good homogeneity (Figure S6). Surface analysis of the prepared FP-MP arrays was carried out using **X-ray photoelectron spectroscopy (XPS)** (Figure 1g). The P 2p_{3/2} and 2p_{1/2} peaks, caused by spin-orbit splitting, were located at binding energies of 129.6 eV and 130.5 eV, respectively, and a weak signal resulting from a small amount of surface oxidation during the test was observed.^[4c, 6a] The successful preparation of FP micro-nano structures predicted the possibility of bottom-up synthesis of other crystalline phosphorus allomers, which was reported from theoretical calculations of crystal structures to experiments according to Roth, Böcker and Häser et al.^[1b, 8-9]

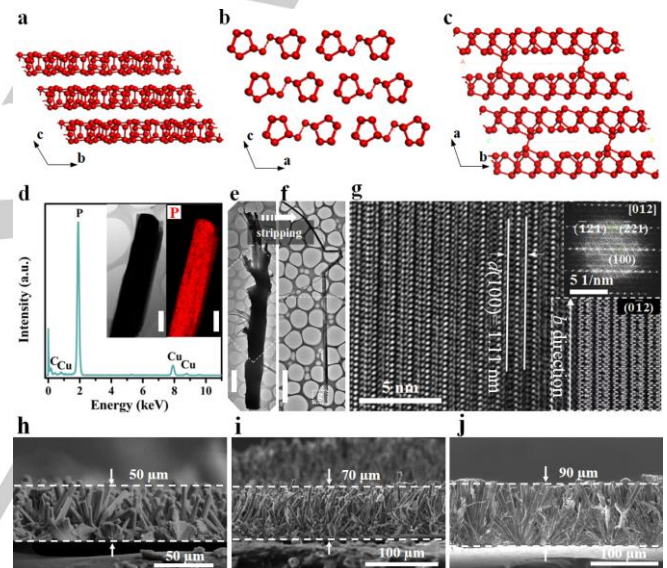


Figure 2. Structural characterisation of FP-MP. Schematic views of FP structure along the crystallographic *a* (a), *b* (b), and *c* (c) directions. (d) The EDS results (main panel) and elemental mapping (inset) of individual FP-MP acquired using a HAADF-TEM instrument. (e) Composite TEM image of the FP-MP. (f) Composite TEM image of the nanoribbon structure of FP-MPs after liquid phase exfoliation treatment. (g) HRTEM image of the white region in f. The upper-right inset shows the FFT of the image, and the three points near the centre correspond to interplanar spacings of 1.11 nm, 0.35 nm, and 0.39 nm, respectively, assigned to the (100), (-121), and (-221) planes of FP.^[3a] The bottom-right overlay shows a schematic of the atomic structure in the FP (0-12) plane. (h - j) SEM images of FP-MP array cross sections of different lengths.

The FP crystal structure consists of pairs of pentagonal phosphorus tube bundles aligned parallel to the crystallographic *b* direction, bound to each other in the *a* and *c* directions by weak vdW interactions (Figure 2a-c).^[1c, 3b, 8] A single FP-MP was placed on a **Transmission Electron Microscopy (TEM)** grid to characterise its crystal structure. The **Energy-Dispersive X-ray Spectroscopy (EDS)** results (Figure 2d) include no signals other than those of elemental phosphorus and the TEM copper grid,

indicating the high purity of the FP-MPs. Moreover, the EDS map shows that phosphorus is uniformly distributed across the array. Due to the fact that the electron beam was not able to penetrate micrometre thicknesses, the FP-MPs underwent liquid-phase exfoliation before their crystal structure was studied. Interestingly, all FP-MPs observed in the field of view were torn longitudinally (Figure 2f and Figure S7), which may be due to the weaker vdW forces in the *a* and *c* directions being disrupted first, while the large aspect ratio also suggests selective growth of the FP-MPs in the longitudinal direction. **High-resolution Transmission Electron Microscopy (HRTEM)** images of the exfoliated FP nanoribbons reveal the defect-free atomic-scale crystal structure and the signature parallel FP lattice stripes (Figure 2g), where the 1.11-nm spacing corresponds to the (100) inter-plane distance of the FP crystal.^[3b] The indices of the reflection points in the corresponding **Fast Fourier Transform (FFT)** pattern indicate that the HRTEM image in Figure 2f was taken along the [0-12] zone axis, which is approximately perpendicular to the *b* direction of FP. Combined with the structural schematic of the (0-12) plane, it can be inferred that the FP-MPs grow in the direction of the *b* axis, i.e. the growth rate in the *b* direction is greater than that in the *a* and *c* directions. As a result, the fibrous phosphorus forms the morphology of micro-pillars. Specifically, different lengths of FP-MP arrays are shown in Figure 2h-j, whereby the length-to-diameter ratio (Figure S8) can be inferred that the growth rate in the *b*-direction is about 14 times greater than that in the *a*- and *c*-directions.

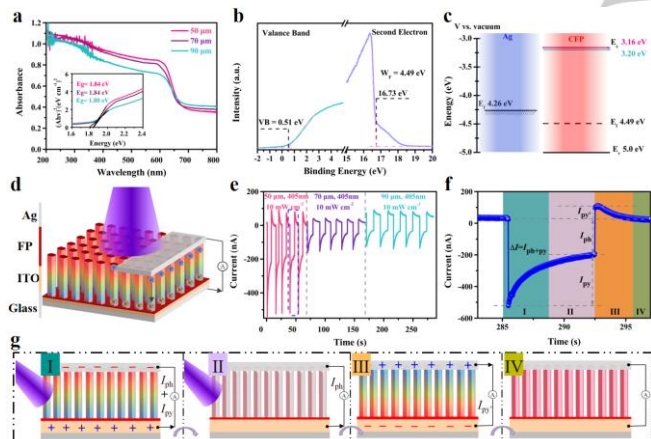


Figure 3. Structure, characterization and operating mechanism of self-powered FP/Ag Schottky junction PD. (a) UV-Vis DRS spectra of the FP-MP arrays. The inset is Kubelka-Munk plots derived from these spectra. (b) Work function and valence band edge of the FP-MP array. (c) Positions of the E_{CB} and E_{VB} of FP on the absolute vacuum energy scale and the work function of Ag. (d) Schematic illustration of self-powered FP/Ag Schottky-junction PD. (e) Photoresponse behaviors of the 50 μm , 70 μm , 90 μm FP-MPs self-powered PD under 405 nm laser illumination at 0 V bias voltage. (f) Expanded view of the single period of the $I-t$ curve indicated by the red dashed outline in e. (g) Schematic diagram of the photoelectric response mechanism of FP/Ag PD in a single cycle of the $I-t$ curve corresponding to the four regions in f.

As evidence for further structural characterization, the structural properties of FP-MPs were measured by UV-Vis diffuse reflectance spectroscopy (DRS) (Figure 3a). Together, these samples have a broad and intense absorption throughout the visible region. Kubelka-Munk plots of the samples show

band gaps around 1.84 eV for FP-MPs of different lengths, where minor differences in band gaps can be attributed to variations in the number and thickness of P layers in dissimilar phases compared to previous reports.^[10] Then, ultraviolet photoelectron spectroscopy (UPS) measurements were performed to obtain information about the energy band alignment of FP-MPs (Figure 3b). The work function (W_F) of FP-MPs was obtained as -4.49 eV by subtracting the second electron cutoff energy from the optical energy of the He I source (21.22 eV). Furthermore, the valence band (VB) edge of FP is 0.51 eV, which is below its Fermi energy level.^[11] Therefore, the energy band diagram in Figure 3f is presented based on the band gap of FP-MPs and the above estimated work function and valence band positions. On this basis, the P-type characteristics and physical properties of FPs are further confirmed with the negative slope of the Mott-Schott curve (Figure S10) and the results of the Hall test (Table S2).

Considering the conditions required for Schottky junction formation and the work function of FP (Figure 3c), self-powered PD with FP/Ag Schottky junctions were fabricated to study the optoelectronic properties of FP-MP arrays.^[12] The self-powered PD composed of FP-MPs is shown in Figure 3d, with details of the preparation process available in the experimental section. The Current-voltage ($I-V$) characteristics of the PD indicate significant optoelectronic effects at 405 nm laser irradiation, for which the PD can operate without bias voltage (Figure S11). Notably, the transient response curves of FP-MP PDs of different lengths all displayed significant pyroelectric current peaks.^[12a, 13] Further, the FP-MP surface absorbs UV light which then generates heat (Figure S13), whereby it is considered as the pyro-phototronic material.^[13b, 14] Analogous to the pyroelectric effect of the p-n junction PD,^[15] the transient response of the PD (region I, Figure 3f, g) is attributed to the coupling of the photoelectric effect (current, I_{ph}) of the Schottky junction with the pyro-phototronic effect (current, I_{py}) of the FP-MPs. Once the temperature of the FP-MPs stabilizes under laser irradiation, the response current is maintained by the photoelectric effect (I_{ph} , region II) alone. However, there appeared reverse pyroelectric charge distribution (region III) on FP-MPs when the temperature suddenly dropped after turning off the light source. Finally, the response current approaches the dark current with the temperature stabilization (region IV) in the absence of illumination.^[12a, 13, 15b, 16]

As shown in Figure 3e, the photoresponses of FP-MP PDs of different lengths are exhibited pyroelectric enhancement effect under 405 nm laser irradiation of power density of 10 mW cm^{-2} . In contrast to the 70 μm and 90 μm FP-MP PDs, the 50 μm FP-MP has shown considerably better photoresponse behavior and detection rate (Figure S18) since thermal absorption and conduction of the 50 μm FP-MP arose more sensitively (Figure S19). Moreover, the photoresponse behavior of the self-powered FP/Ag Schottky junction PD under 405, 655 and 980 nm laser irradiation (Figure 4a) exhibited broadband response from violet to near-infrared wavelengths. Compared to the photoresponse at 980 nm (≈ 9.2 nA), the I_{py+ph} at 405 and 655 nm (≈ 0.3 & 0.1 μA) was higher due to the presence of photogenerated carriers.^[17] It is worth noting that different wavelengths of laser light have different effects on the self-powered FP/Ag Schottky PD, with the operating mechanism shown in Figure 4b. The interface between the FP-MP and Ag electrodes formed the Schottky barrier. The transient pyroelectric current would be

generated rapidly inside the FP-MP under light illumination. Meanwhile, the pyroelectric potential would also be generated inside the FP-MP due to the temperature increase, which reduced the height of the Schottky barrier at the interface. Although the 980 nm laser illumination beyond the absorption range of the FP led to the inability to generate photogenerated carriers, the pyroelectric effect still caused the generation of pyroelectric charge formation enhancement factor, which resulted in the rise or fall of the output current.

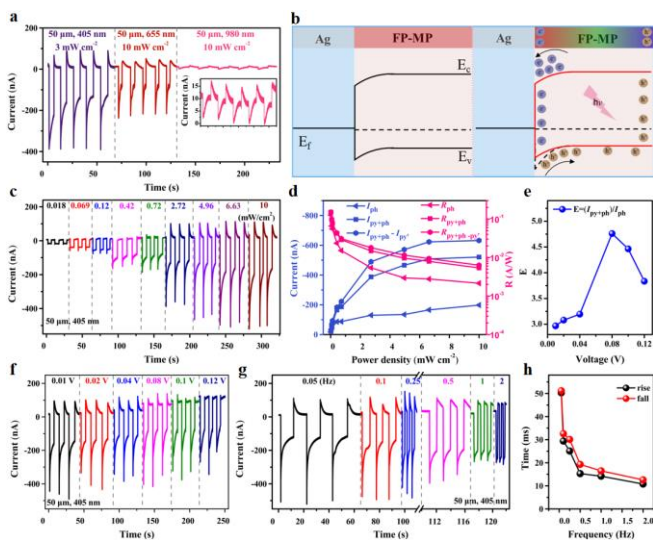


Figure 4. Pyro-phototronic effect of self-powered FP/Ag Schottky junction PD. (a) Photoresponse behaviors of the 50 μm FP-MPs self-powered PD under 405, 655 and 980 nm laser illumination at 0 V bias voltage. The inset is the enlarged photoresponse for 980 nm laser illumination. (b) Band maps of self-powered FP/Ag Schottky junction under dark (left) and light (right) conditions. (c) I - t characteristics of the 50 μm FP-MP PD under 405 nm laser illumination with different optical intensities in the range of 0.018 ~ 10 mW/cm^2 . (d) $I_{\text{py+ph}}$, I_{ph} and $I_{\text{py-ph}} - I_{\text{py}}$ & $R_{\text{py+ph}}$, R_{ph} and $R_{\text{py+ph-py}}$ of self-powered PDs as a function of power density. (e) Corresponding enhancement factor $E = (I_{\text{py+ph}})/I_{\text{ph}}$ of self-powered PD as a function of bias voltage. (f) I - t characteristics of self-powered PD at 0.1 Hz for different bias voltages of 0.01 V ~ 0.12 V (power density ~ 10 mW/cm^2). (g) I - t characteristics of the self-powered PD at different frequencies from 0.05 ~ 2 Hz (power density ~ 10 mW/cm^2). (h) Corresponding rise and fall times of the self-powered PD as a function of frequency.

The photoresponse of the self-powered FP/Ag Schottky junction PD showed excellent pyroelectric effects at zero bias voltage under 405 nm laser irradiation of power densities 0.018 ~ 10.0 mW/cm^2 , as shown in Figure 4c. The maximum enhancement factors of $R_{\text{py+ph-py}}/R_{\text{ph}}$ and $R_{\text{py+ph}}/R_{\text{ph}}$ were 3.90 and 3.26, respectively, at a power density of 4.96 mW/cm^2 (Figure 4c). Being the key parameter of PD, the maximum values of responsiveness $R_{\text{py+ph}}$ and detection rate $D^*_{\text{py+ph}}$ were 151.03 mA/W and 3.50×10^9 , respectively, at laser intensity of 0.018 mW/cm^2 (Figure 4d, S18). As shown in Figure 4f, the photocurrent and dark current gradually increase with increasing bias voltage, while $I_{\text{py+ph}}$ and I_{py} gradually decrease under 405 nm illumination at a power density of 10 mW/cm^2 and 0.1 Hz. On the other hand, the enhancement factor E ($I_{\text{py+ph}}/I_{\text{ph}}$) decreases with the increase of the bias voltage, indicating that the Joule heat generated by the applied bias voltage weakens the pyroelectric effect. In addition, $I_{\text{py+ph}}$ decreases with frequency (Figure 4g), however, the response rate increases with frequency due to the enhanced rate of temperature change

at higher frequencies under 405 nm laser irradiation with a power density of 10.0 mW/cm^2 . Together, these results revealed that the pyroelectric effect is controllable by external conditions such as illumination frequency and applied bias voltage. Moreover, similar results were obtained for different lengths of FP-MP & under 655 and 980 nm laser illumination shown in Figures S14-S17 & S20-S24 in the Supporting Information, respectively.

In summary, we have achieved bottom-up synthesis of FP-MP arrays with novel physical properties on the centimeter scale by the LP-CVT method. Subsequently, a self-powered PD based on the FP/Ag Schottky structure was fabricated, which achieved a broadband response from violet (405 nm) to NIR (980 nm) under zero-bias conditions, even exceeding the bandgap limit of FP. These excellent optoelectronic properties were attributed to the coupling of the pyro-phototronic and photovoltaic effects of FP-MPs. Further, the operating mechanism of different laser illumination and the effects of light frequency and applied bias voltage on the pyroelectric effect were investigated. What we have done raises the possibility of further development of FP-based wafer-scale optoelectronic and electronic devices.

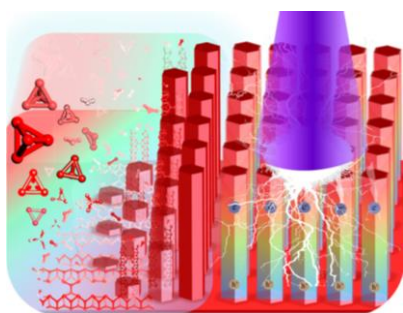
Acknowledgements

This work was supported by the National Natural Science Foundation of China (21972103) and SHANXI-ZHEDA Institute of Advanced Materials and Chemical Engineering (2021SX-AT007).

Keywords: two dimensional semiconductor material • top-down synthesis • fibrous phosphorus • pyro-phototronic effect • photodetectors

- [1] a) A. Carvalho, M. Wang, X. Zhu, A. S. Rodin, H. Su, A. H. Castro Neto, *Nature Reviews Materials* **2016**, *1*, 1-16; b) W. L. Roth, W. T. De, A. J. Smith, *J Am Chem Soc* **1947**, *69*, 2881-2885; c) L. Du, Y. Zhao, L. Wu, X. Hu, L. Yao, Y. Wang, X. Bai, Y. Dai, J. Qiao, M. G. Uddin, X. Li, J. Lahtinen, X. Bai, G. Zhang, W. Ji, Z. Sun, *Nat Commun* **2021**, *12*, 4822; d) Z. Hu, L. Yuan, Z. Liu, Z. Shen, J. C. Yu, *Angew Chem Int Ed Engl* **2016**, *55*, 9580-9585; e) J. B. Smith, D. Hagaman, D. DiGuseppi, R. Schweitzer-Stenner, H. Ji, *Angew Chem Int Ed Engl* **2016**, *128*, 12008-12012; f) Q. Liu, X. Zhang, J. Wang, Y. Zhang, S. Bian, Z. Cheng, N. Kang, H. Huang, S. Gu, Y. Wang, D. Liu, P. K. Chu, X. F. Yu, *Angew Chem Int Ed Engl* **2020**, *59*, 14383-14387.
- [2] a) Z. Wu, Y. Lyu, Y. Zhang, R. Ding, B. Zheng, Z. Yang, S. P. Lau, X. H. Chen, J. Hao, *Nat Mater* **2021**, *20*, 1203-1209; b) Y. Xu, X. Shi, Y. Zhang, H. Zhang, Q. Zhang, Z. Huang, X. Xu, J. Guo, H. Zhang, L. Sun, Z. Zeng, A. Pan, K. Zhang, *Nature Communications* **2020**, *11*, 1-8; c) C. Li, Y. Wu, B. Deng, Y. Xie, Q. Guo, S. Yuan, X. Chen, M. Bhuiyan, Z. Wu, K. Watanabe, T. Taniguchi, H. Wang, J. J. Cha, M. Snure, Y. Fei, F. Xia, *Advanced Materials* **2018**, *30*, 1703748; d) L. Zhang, H. Huang, B. Zhang, M. Gu, D. Zhao, X. Zhao, L. Li, J. Zhou, K. Wu, Y. Cheng, J. Zhang, *Angew Chem Int Ed Engl* **2020**, *59*, 1074-1080; e) Z. Sun, B. Zhang, Y. Zhao, M. Khurram, Q. Yan, *Chemistry of Materials* **2021**, *33*, 6240-6248.
- [3] a) A. Pfitzner, *Angew Chem Int Ed Engl* **2006**, *45*, 699-700; b) N. Eckstein, A. Hohmann, R. Wehrich, T. Nilges, P. Schmidt, *Zeitschrift für anorganische und allgemeine Chemie* **2013**, *639*, 2741-2743; c) C. Wu, R. Zhu, W. Y. Teoh, Y. Liu, J. Deng, H. Dai, L. Jing, Y. H. Ng, J. C. Yu, *Applied Catalysis B: Environmental* **2022**, *312*, 121428.

- [4] a) Z. Hu, W. Guo, *Small* **2021**, *17*, e2008004; b) Z. Chen, Y. Zhu, Q. Wang, W. Liu, Y. Cui, X. Tao, D. Zhang, *Electrochimica Acta* **2019**, *295*, 230-236; c) S. Li, Y. H. Ng, R. Zhu, S. Lv, C. Wu, Y. Liu, L. Jing, J. Deng, H. Dai, *Applied Catalysis B: Environmental* **2021**, *297*, 120412.
- [5] R. A. Winchester, M. Whitby, M. S. Shaffer, *Angew Chem Int Ed Engl* **2009**, *48*, 3616-3621.
- [6] a) M. C. Watts, L. Picco, F. S. Russell-Pavier, P. L. Cullen, T. S. Miller, S. P. Bartus, O. D. Payton, N. T. Skipper, V. Tileli, C. A. Howard, *Nature* **2019**, *568*, 216-220; b) D. Zhou, H. Li, N. Si, H. Li, H. Fuchs, T. Niu, *Advanced Functional Materials* **2020**, *31*, 2006997.
- [7] S. Zhang, S. Ma, X. Hao, Y. Wang, B. Cao, B. Han, H. Zhang, X. Kong, B. Xu, *Nanoscale* **2021**, *13*, 18955-18960.
- [8] M. Ruck, D. Hoppe, B. Wahl, P. Simon, Y. Wang, G. Seifert, *Angew Chem Int Ed Engl* **2005**, *44*, 7616-7619.
- [9] S. Böcker, M. Häser, *Zeitschrift für anorganische und allgemeine Chemie* **1995**, *621*, 258-286.
- [10] F. Liu, R. Shi, Z. Wang, Y. Weng, C. M. Che, Y. Chen, *Angew Chem Int Ed Engl* **2019**, *58*, 11791-11795.
- [11] a) P. Luo, F. Wang, J. Qu, K. Liu, X. Hu, K. Liu, T. Zhai, *Advanced Functional Materials* **2020**, *31*, 2008351; b) B. Cao, Q. Liu, Y. Zheng, X. Tang, J. Chai, S. Ma, W. Wang, G. Li, *Advanced Functional Materials* **2022**, *32*, 2110715.
- [12] a) Y. Wang, L. Zhu, Y. Feng, Z. Wang, Z. L. Wang, *Advanced Functional Materials* **2018**, *29*, 1807111; b) D. Xiang, C. Han, Z. Hu, B. Lei, Y. Liu, L. Wang, W. P. Hu, W. Chen, *Small* **2015**, *11*, 4829-4836.
- [13] a) A. K. Rana, M. Kumar, D. K. Ban, C. P. Wong, J. Yi, J. Kim, *Advanced Electronic Materials* **2019**, *5*, 1900438; b) P. Wan, M. Jiang, T. Xu, Y. Liu, X. Fang, C. Kan, *Advanced Optical Materials* **2021**, *10*, 2101851.
- [14] M. Kumar, M. Patel, G.-N. Lee, J. Kim, *ACS Applied Nano Materials* **2017**, *1*, 319-324.
- [15] a) W. Yang, J. Chen, Y. Zhang, Y. Zhang, J. H. He, X. Fang, *Advanced Functional Materials* **2019**, *29*, 1808182; b) Q. Li, J. Meng, J. Huang, Z. Li, *Advanced Functional Materials* **2021**, *32*, 2108903.
- [16] a) B. Ouyang, K. Zhang, Y. Yang, *iScience* **2018**, *1*, 16-23; b) D. You, C. Xu, W. Zhang, J. Zhao, F. Qin, Z. Shi, *Nano Energy* **2019**, *62*, 310-318.
- [17] Y. Dai, X. Wang, W. Peng, C. Xu, C. Wu, K. Dong, R. Liu, Z. L. Wang, *Adv Mater* **2018**, *30*, 1705893.



Directed transformations of amorphous red phosphorus (ARP) structures lead to the self-assembled synthesis of high-quality, large-scale fibrous phosphorus micropillar (FP-MP) arrays with pyro-phototronic effects.